

## Doped semiconducting polymer nanoantennas for tunable organic plasmonics

Akchheta Karki<sup>1</sup>, Yu Yamashita<sup>2,3</sup>, Shangzhi Chen<sup>1</sup>, Tadanori Kurosawa<sup>2</sup>, Jun Takeya<sup>2,3</sup>, Vallery Stanishev<sup>4</sup>, Vanya Darakchieva<sup>4,5,6</sup>, Shun Watanabe<sup>2</sup> & Magnus P. Jonsson<sup>1</sup>✉

Optical nanoantennas are often based on plasmonic resonances in metal nanostructures, but their dynamic tunability is limited due to the fixed permittivity of conventional metals. Recently, we introduced PEDOT-based conducting polymers as an alternative materials platform for dynamic plasmonics and metasurfaces. Here, we expand dynamic organic plasmonic systems to a wider class of doped polythiophene-based semiconducting polymers. We present nanodisks of PBTTT semiconducting polymer doped with a dicationic salt, enabling a high doping level of around 0.8 charges per monomer, and demonstrate that they can be used as nanooptical antennas via redox-tunable plasmonic resonances. The resonances arise from the polymer being optically metallic in its doped state and dielectric in its non-conducting undoped state. The plasmonic resonances are controllable over a 1000 nm wavelength range by changing the dimensions of the nanodisks. Furthermore, the optical response of the nanoantennas can be reversibly tuned by modulating the doping level of the polymer. Simulations corroborate the experimental results and reveal the possibility to also modulate the optical nearfield response of the nanoantennas.

<sup>1</sup>Laboratory of Organic Electronics, Department of Science and Technology (ITN), Linköping University, Norrköping SE-601 74, Sweden. <sup>2</sup>Material Innovation Research Center (MIRC), Department of Advanced Materials Science, Graduate School of Frontier Sciences, The University of Tokyo, 5-1-5 Kashiwanoha, Kashiwa, Chiba 277-8561, Japan. <sup>3</sup>International Center for Materials Nanoarchitectonics (WPI-MANA), National Institute for Materials Science (NIMS), 1-1 Namiki, Tsukuba 305-0044, Japan. <sup>4</sup>Terahertz Materials Analysis Center (THeMAC), Department of Physics, Chemistry and Biology (IFM), Linköping University, Linköping SE-581 83, Sweden. <sup>5</sup>Center for III-Nitride Technology, C3NiT-Janzèn, Department of Physics, Chemistry and Biology (IFM), Linköping University, Linköping SE-581 83, Sweden. <sup>6</sup>Solid State Physics and NanoLund, Lund University, S-221 00 Lund, Sweden. ✉email: [magnus.jonsson@liu.se](mailto:magnus.jonsson@liu.se)

Conventional plasmonics is based on metal nanostructures, which can be used as optical nanoantennas to control light at the nanoscale<sup>1</sup>. As a result, such systems have been widely utilized in areas including energy conversion<sup>2–4</sup>, biosensing<sup>5–9</sup>, display technologies<sup>10–13</sup>, ultrathin optical components<sup>14–18</sup>, and many others. However, the tunability of such metallic nanostructures is limited due to the fixed permittivity of conventional metals<sup>19</sup>. This has led to an increased interest in nanoantennas based on materials with tunable properties, such as phase-change materials<sup>20–24</sup>, doped metal oxide nanocrystals<sup>25</sup>, and graphene<sup>26–28</sup>. We recently reported the first demonstration of poly(3,4-ethylenedioxythiophene) (PEDOT) based conducting polymers as a new type of material for dynamic organic plasmonics, with the polymer acting as an intrinsically plasmonic material due to its high density of mobile polaronic charge carriers ( $2.6 \times 10^{21} \text{ cm}^{-3}$ , determined by ellipsometry)<sup>29</sup>. As of yet, dynamic organic plasmonics has only been demonstrated in PEDOT-based polymers<sup>29–31</sup>. Here, we show the possibility to expand dynamic organic plasmonic systems to another class of doped polythiophene-based semiconducting polymers.

The ability to precisely and reproducibly dope organic semiconductors is vital for their use in electronic devices. Molecular doping, which uses redox-active molecules as dopants for organic semiconductors, has several drawbacks due to the dopant molecule having to undergo both the charge transfer and compensation steps<sup>32</sup>. Therefore, such devices generally have poor stability and reproducibility, making their commercialization difficult<sup>32–34</sup>. A doping technique based on dicationic salts provided a breakthrough in the field, as demonstrated by doping the semiconducting polymer poly[2,5-bis(3-tetradecylthiophen-2-yl)thieno[3,2-b]thiophene] (PBTtT) using the dopant N4,N4,N4',N4'-Tetrakis(4-bromophenyl)-[1,1'-biphenyl]-4,4'-diammonium di[bis(trifluoromethylsulfonyl)imide] (TAB-2TFSI)<sup>33</sup>. Such salts of dicationic species were shown to dope the semicrystalline polymer PBTtT at the highest possible doping level of close to one charge per monomer, yielding high charge carrier density ( $n \approx 1.9 \times 10^{21} \text{ cm}^{-3}$  from Hall effect measurements) and mobility ( $\mu = 1.6 \text{ cm}^2 \text{ V}^{-1} \text{ s}^{-1}$  from Hall effect measurements), as well as good atmospheric stability<sup>33</sup>.

We demonstrate here that PBTtT polymers doped using this method can have sufficiently high charge density and mobility to attain negative permittivity. The polymer thereby behaves optically as a metal in its doped state. Using nanodisks as model system, we show that this enables the polymer to be used as a plasmonic material for nano-optical nanoantennas, with resonances controllable over a 1000 nm wavelength range by simply changing the dimensions of the nanodisks. Importantly, the polymer remains dielectric in its non-conducting undoped state. Plasmonic resonances in such devices can therefore be reversibly turned on/off or tuned by modulating the polymer doping level. Importantly, this work opens the possibility to explore a plethora of other already existing similarly doped semiconducting polymers for their potential in organic plasmonics and nano-optics<sup>32–38</sup>.

## Results

**Doped PBTtT optical nanoantennas.** Figure 1a illustrates the process of doping PBTtT films with the TAB-2TFSI dopant<sup>33</sup>. The TAB-2TFSI dopant is dissolved in acetonitrile where upon dissolution, the dopant dissociates into one  $\text{TAB}^{2+}$  dication and two  $\text{TFSI}^-$  anions. When the TAB-2TFSI dopant solution encounters the undoped PBTtT film, the doping process ensues. As  $\text{TAB}^{2+}$  is a strong oxidant, there is an immediate electron transfer from the PBTtT polymer to  $\text{TAB}^{2+}$ <sup>33</sup>. This reaction reduces  $\text{TAB}^{2+}$  to its radical cation form  $\text{TAB}^{\bullet+}$  and oxidizes the neutral PBTtT polymer to its radical cation (polaron) form

( $\text{PBTtT}^{\bullet+}$ )<sup>33</sup>. To counterbalance the positively charged radical cation (polaron) of the PBTtT, one of the  $\text{TFSI}^-$  anions diffuses into the polymer film while the other  $\text{TFSI}^-$  anion remains in the acetonitrile solution to stabilize the radical cation  $\text{TAB}^{\bullet+}$ <sup>33</sup>. The overall doping reaction process can be summarized as follows:

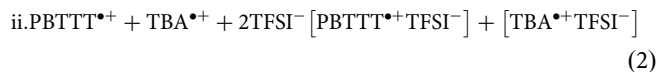
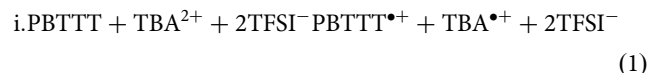
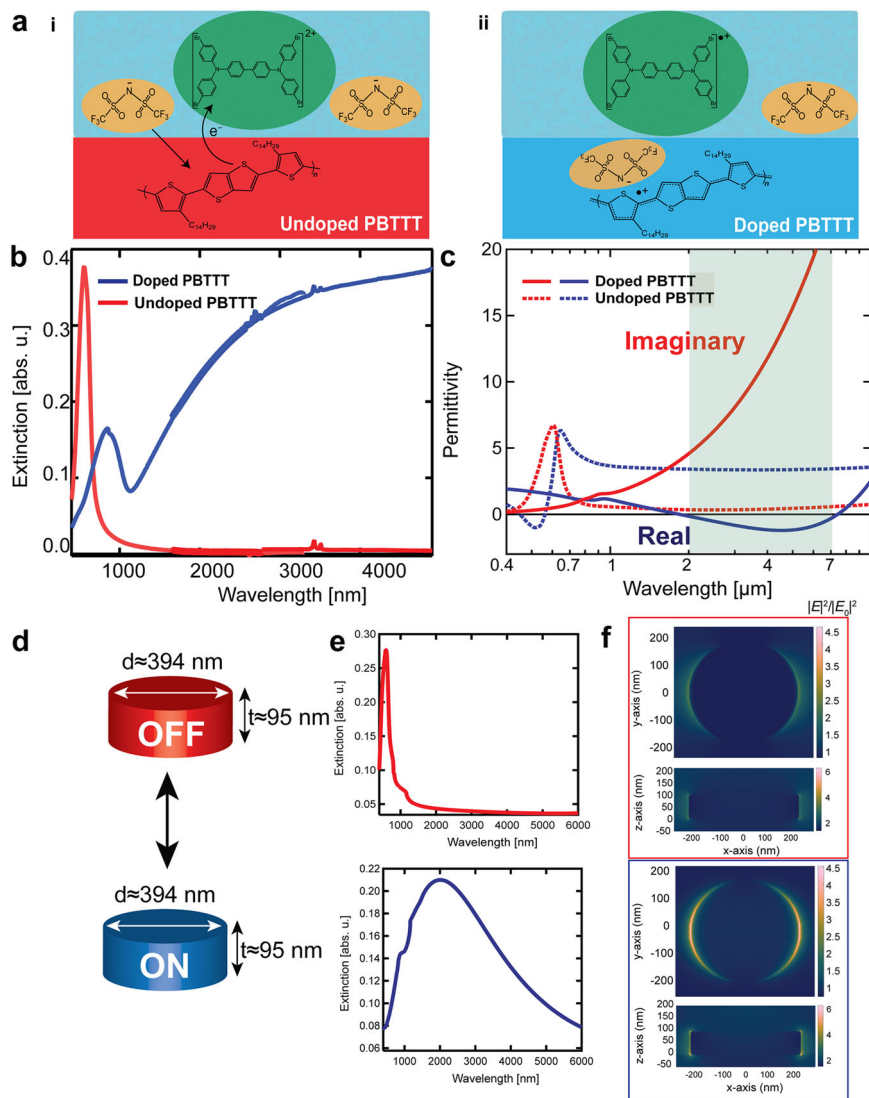


Figure 1b presents absorption spectra of a PBTtT film before and after doping with TAB-2TFSI. As expected, the doped PBTtT film showed free carrier absorption in the infrared region and a clear lower oxidation level polaronic absorption peak at around  $\sim 900 \text{ nm}$ <sup>33</sup>. These features were completely lacking for the undoped PBTtT film, which instead showed an absorption peak at  $\sim 590 \text{ nm}$  originating from the neutral PBTtT polymer. As a result, successful doping led to a change in color of the PBTtT film from dark red (undoped) to light blue (doped) (Supplementary Fig. 1c). We further confirmed that PBTtT films of three different thicknesses ( $\sim 36 \text{ nm}$ ,  $\sim 60 \text{ nm}$ , and  $\sim 95 \text{ nm}$ ) made from dissolving 1, 1.5, and 2 weight percent (wt%) of PBTtT powders in dichlorobenzene undergo such a doping process (Supplementary Fig. 1a). Simulations (based on measured permittivity of undoped and doped PBTtT) show good agreement with the experimentally measured results (Supplementary Fig. 1b).

Importantly, doping introduces a high density of mobile charge carriers<sup>33</sup>, with conductivities exceeding  $400 \text{ S/cm}$ . In Fig. 1c, we show that this makes this semicrystalline polymer optically metallic in the infrared, forming the basis for using the material for plasmonic nanoantennas. Figure 1c compares the in-plane permittivity of doped and undoped PBTtT films, showing a clear transition between metallic (negative real permittivity) and dielectric (positive real permittivity) response measured via ellipsometry. Supplementary Figs. 2–4 and Tables S1, S2 contain the raw ellipsometry data and fitting parameters. The doped PBTtT film provides negative real permittivity in the spectral region from  $\sim 2\text{--}7 \mu\text{m}$ , making the material metallic in this region<sup>29,30</sup>. Contrastingly, the undoped PBTtT film instead shows positive permittivity in the same spectral region, presenting an opportunity to tune this material between its metallic and dielectric behavior. This gives promise for using nanostructures of the material as tunable plasmonic nanoantennas.

Figure 1d–f present optical simulation results for undoped (top row) and doped (bottom row) PBTtT nanodisk arrays, with the nanostructure geometry shown in panel d. The top red curve in Fig. 1e presents the simulated optical extinction of an undoped PBTtT nanodisk array, which only shows the signature peak of the neutral PBTtT polymer also seen in the film. There is no indication of any plasmonic resonance for this undoped PBTtT nanostructure. By contrast, the simulated optical extinction of a doped PBTtT nanodisk array with the same geometry (blue curve) shows a clear resonance peak at  $\sim 2011 \text{ nm}$ . We attribute this peak to a plasmonic dipolar resonance in the metallic polymer nanodisks. The small shoulder at  $\sim 900 \text{ nm}$  is not a plasmonic resonance, but a lower oxidation level polaronic peak as also present for the non-structured doped film. Figure 1f compares optical near-field profiles of a single undoped and doped PBTtT nanodisk (at the resonance wavelength of  $\sim 2011 \text{ nm}$ ), confirming the dipolar nature of the resonance and showing that the electric fields around the nanoantennas are significantly higher in the doped state than in the undoped state.



**Fig. 1** Concept of doped PBTTT polymer nanoantennas. **a** Doping mechanism of PBTTT films with the TAB-2TFSI dopant. **b** Absorption spectra of films made from 1.5 wt% PBTTT (thickness  $\approx 60$  nm) in the doped (blue) and undoped (red) states. **c** In-plane permittivity dispersion of PBTTT in its doped (blue curve, real part; red curve, imaginary part) and undoped (dashed blue curve, real part; dashed red curve, imaginary part) states. The spectral range between  $\approx 2$  and  $7 \mu\text{m}$  is defined as a metallic regime where the real permittivity is below zero for the doped polymer. **d** Dimensions of doped and undoped PBTTT nanodisk arrays on glass substrates used to simulate the extinction and near field profiles in **e** and **f**. **e** Simulated extinction and **f** nearfield response for nanodisk arrays (diameter = 394 nm, thickness = 95 nm, period = 800 nm, mesh size =  $2 \times 2 \times 2 \text{ nm}^3$  around the nanodisks) at the resonance peak wavelength of  $\sim 2011$  nm, based on doped (blue) and undoped (red) PBTTT nanodisks. In (**f**), top panels are top views while bottom panels are cross sections of the nanodisks along the direction of the incident polarization, which is along the  $x$ -axis.  $x$ - $y$  in-plane direction is 2 nm above the nanodisk and  $x$ - $z$  cross-section is through the center of the nanodisk. The color scale bars show the square of the electric field strength relative to the incident light ( $|E|^2/|E_0|^2$ ).

**Controlling the plasmonic resonance position via nanodisk dimensions.** To experimentally confirm the excitation of plasmons in doped PBTTT polymer nanostructures and demonstrate tuning of their nanooptical response, we fabricated sparse arrays of PBTTT nanodisks of different dimensions on glass substrates using a modified version of colloidal lithography (see Fig. 2a). In brief (see Supplementary Fig. 6 and Methods for details), we deposited polystyrene (PS) nanoparticles onto undoped PBTTT films (Fig. 2ai-ii). This was followed by oxygen plasma etching to obtain PBTTT nanodisks under the PS nanoparticles (Fig. 2aiii). The PS nanoparticles were then selectively removed so that only the PBTTT nanodisks remained on the substrate (Fig. 2aiv). In a last step, the PBTTT nanodisks were doped by the TAB-2TFSI dopant inside a nitrogen glovebox. It was important to dope the film in a last step as direct contact of the doped films with water,

which occurred during the PS nanoparticle deposition process, de-doped the doped PBTTT films. Additionally, we found it useful to spin-off a few drops of acetonitrile from the substrate to remove excessive dopant adhered to the bare glass between the PBTTT nanodisks (see Supplementary Fig. 5a and Supplementary Fig. 5b). We made around 400 nm diameter nanodisks of different thicknesses ( $\approx 36$  nm,  $\approx 60$  nm,  $\approx 95$  nm) by increasing the weight percent of PBTTT powder in solution (1wt %, 1.5wt %, 2 wt%, respectively). Conductivity measurements confirmed that the material properties of films made at the three different thicknesses were very similar (Table 1). AFM imaging revealed successful fabrication of large areas of PBTTT nanodisks (Supplementary Figs. 7–9a) and was also used to extract representative nanodisk heights and diameters (Supplementary Figs. 7–9b, c).

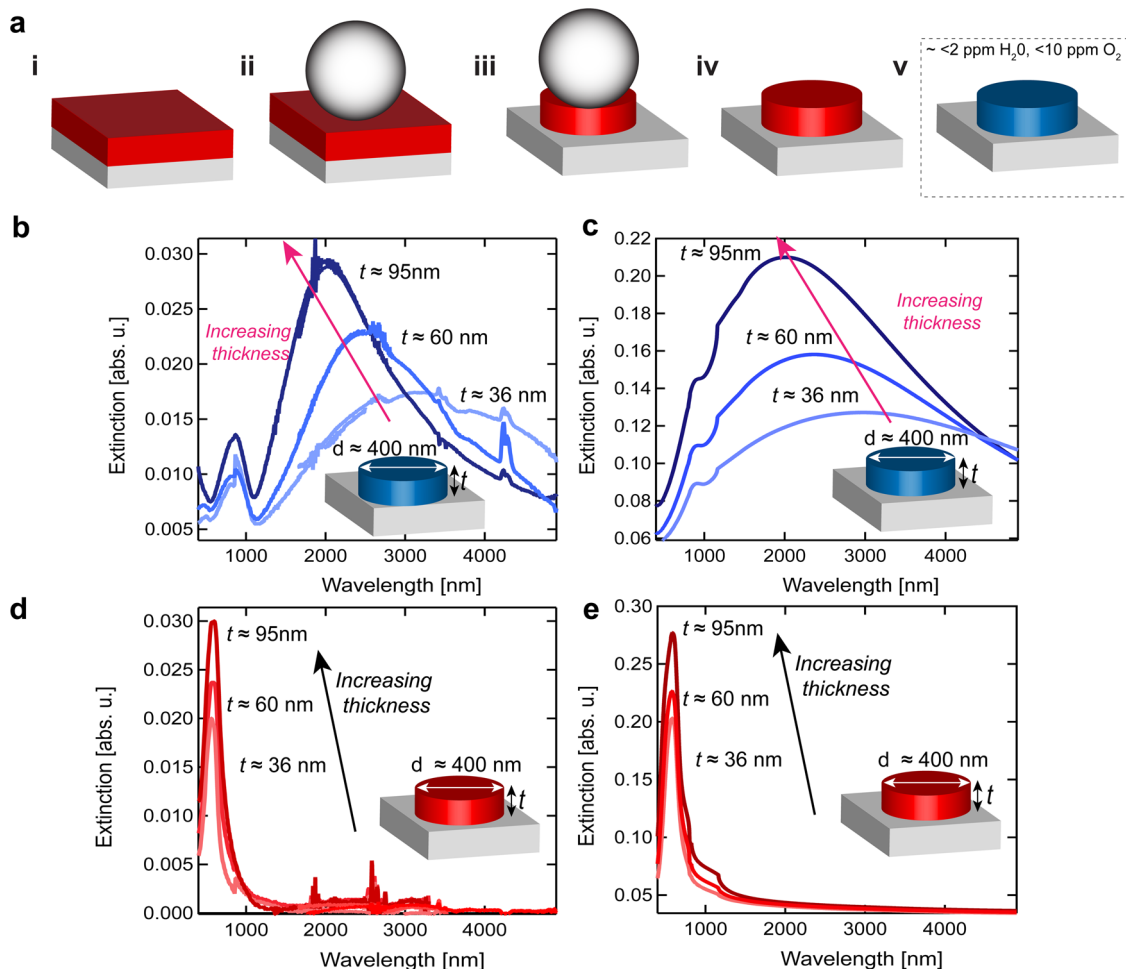


**Fig. 2 Resonance-tuning by nanodisk geometry.** **a** Schematic of the fabrication process of PBTTT nanodisk arrays based on a modified version of colloidal lithography. **b** Experimental and **c** simulated extinction spectra of undoped PBTTT nanodisks made with dimensions (diameter  $\approx 400$  nm, thicknesses  $\approx 36$  nm,  $60$  nm,  $95$  nm) extracted from AFM height and width analyses (Supplementary Figs. 7–9b, c). **d** Experimental and **e** simulated extinction spectra of doped PBTTT nanodisks made with dimensions (diameters  $\approx 400$  nm, thicknesses  $\approx 36$  nm,  $60$  nm,  $95$  nm, period =  $800$  nm, mesh size =  $2 \times 2 \times 2$  nm<sup>3</sup> around the nanodisks) extracted from AFM height and width analyses (Supplementary Figs. 7–9b, c).

**Table 1 Average conductivity values measured using the 4-point probe method for films made from 1, 1.5, and 2 wt% PBTTT doped with TAB-2TFSI, measured at 10 different spots in a film.**

Sample	Conductivity [S/cm]
1 wt % PBTTT (doped w/TAB-2TFSI)	$437 \pm 40$
1.5 wt% PBTTT (doped w/TAB-2TFSI)	$474 \pm 22$
2 wt% PBTTT (doped w/TAB-2TFSI)	$486 \pm 18$

Doping was done inside a nitrogen glovebox. Conductivity was measured in air within 1 h of exposure to atmosphere.

Excitingly, the doped PBTTT nanodisk samples all showed clear extinction peaks. This shows that this type of material can be used for plasmonic nanoantennas. Sequentially increasing the nanodisk thickness from  $\approx 36$  nm (1 wt% PBTTT), to  $\approx 60$  nm (1.5 wt% PBTTT), and finally  $\approx 95$  nm (2 wt% PBTTT), led to substantial blue shifts in the resonance peak position, from  $\sim 3200$  nm down to  $\sim 2100$  nm (Fig. 2b). Such blue shift with increasing thickness agrees with expectations based on theory as well as previous results for both conventional metal nanodisks and PEDOT nanodisks<sup>29,30,39</sup>. Additionally, the thicker nanodisks resulted in higher extinction signals. Both these trends could

be reproduced by optical simulations, which also match the experimental results in terms of approximate resonance peak wavelengths and relative changes in the extinction (Fig. 2c). Small differences can be due to geometrical variations, inaccuracies in the measured permittivity, and imperfections of the fabricated nanodisks and their coverage on the substrate. Broadening of the simulated plasmonic resonances can be attributed to small variations in the material properties during the time of the ellipsometry measurements, which can take up to 3 days to cover the full UV-Vis and THz spectral ranges. The doped films become slightly de-doped over time when left in normal atmospheric conditions, as shown in Supplementary Fig. 10. These changes are relatively small but may still affect the measured permittivity and lead to broadening of the simulated resonance peaks. As expected, the undoped PBTTT nanodisks (i.e. before doping) did not show any plasmonic resonances (Fig. 2d). Instead, they only show the neutral PBTTT absorption peak at shorter wavelengths with no dependence of peak position on film thickness. Optical simulations of undoped PBTTT nanodisks also confirm these observations (Fig. 2e). Supplementary Fig. 11 presents simulations of doped and undoped nanodisks at varying periods, showing that the peaks remain unchanged with period. They also show the presence of grating features that vary with period.



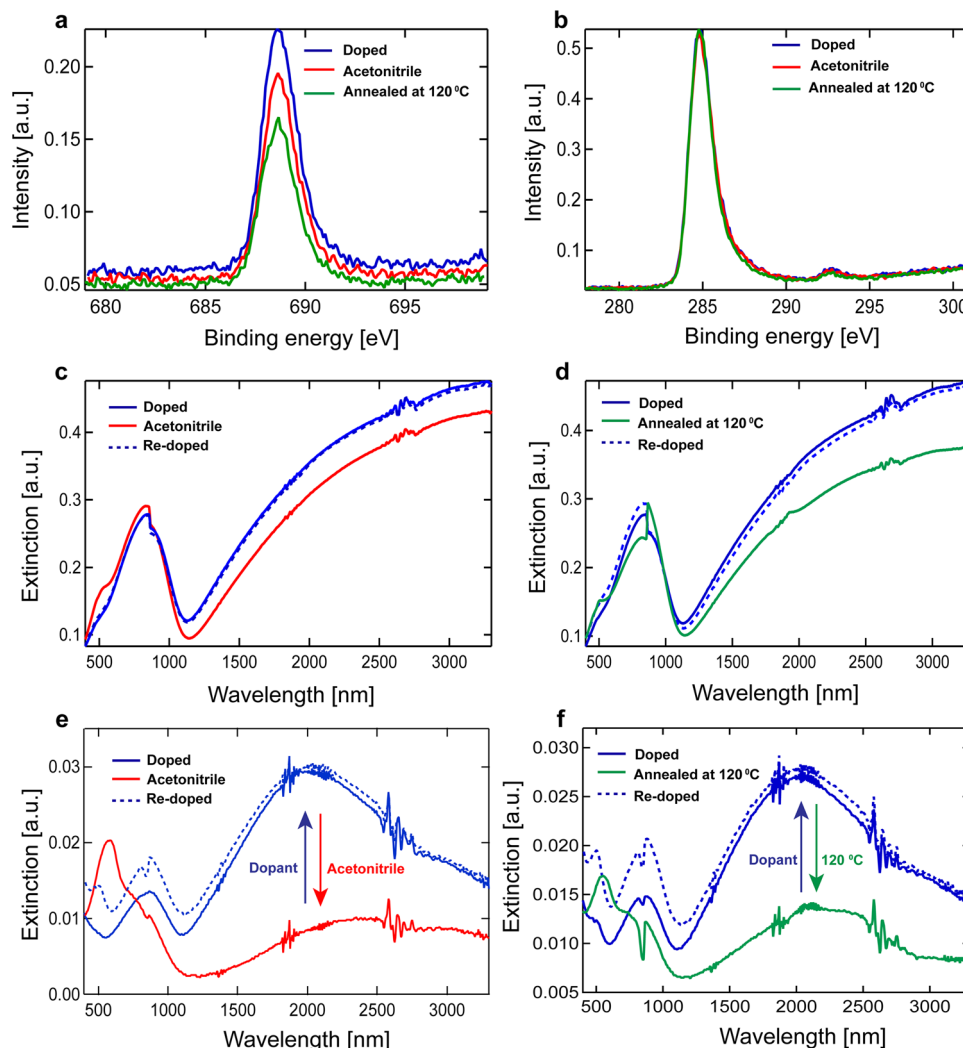


**Fig. 3 Reversible switching of PBTTT nanoantennas.** **a** Fluorine and **b** Carbon XPS spectra of PBTTT films after doping, after acetonitrile de-doping, and 120 °C temperature de-doping. The doping levels can be estimated by the F/C atomic composition ratio as summarized in Table S2. The intensities are normalized based on the intensity of the carbon signal. **c, d** Measured extinction for a thin PBTTT film on glass for **(c)** acetonitrile de-doping and **d** 120 °C temperature de-doping. **e, f** Measured extinction for PBTTT nanodisks on glass (thickness = 95 nm, diameter = 394 nm) for **e** acetonitrile de-doping and **f** 120 °C temperature de-doping.

**Dynamic tunability of the nanooptical response by chemical and temperature treatments.** We will now demonstrate that PBTTT polymer nanoantennas can be repeatedly switched on/off or tuned by varying the doping level of the polymer. Previous studies showed that PBTTT films doped with TAB-2TFSI can be de-doped via acetonitrile or temperature annealing treatments<sup>35</sup>. We confirmed that such treatments can lead to partial de-doping of doped (non-structured) PBTTT films by measuring the doping levels of the films via x-ray photoelectron spectroscopy (XPS). Survey scans of all the atoms present in the film were first measured as shown in Supplementary Fig. 12. High resolution spectra were then obtained in narrow energy ranges to estimate the composition of carbon and fluorine atoms present in the films. Figure 3a shows the fluorine XPS spectra for the films, where the fluorine signal is highest for the doped PBTTT films, followed by the acetonitrile treated film, and then the temperature annealed film. Contrastingly, the carbon XPS spectra for all three films shown in Fig. 3b demonstrate similar signal intensities. The fluorine to carbon (F/C) ratio was then obtained based on the integrated areas under the carbon and fluorine peaks above a linear baseline. As the fluorine atom is only present in the dopant

TAB-2TFSI (see Fig. 1a for chemical structure), the presence of fluorine atoms in the doped PBTTT films comes from the TFSI anions that counterbalance the positively charged radical cation (polaron) of the doped PBTTT films (see equation 2). Hence, the amount of fluorine to carbon atoms in the film should be proportional to the doping level (i.e., anions per monomer) of the film (See Supplementary Table 3 and Supplementary Note 1 for details). Table 2 shows the F/C ratio and the corresponding doping levels for the doped PBTTT films and the acetonitrile-treated and 120 °C annealed de-doped films, confirming that we could lower the doping levels by these treatments. The results are consistent with conductivity measurements of the de-doped films, which was found to be lower after treatments and proportional to the doping levels obtained by XPS. Figure 3c shows experimental extinction spectra of the doped, de-doped, and re-doped films for the acetonitrile de-doping process. The spectra confirm that de-doping with acetonitrile led to a reduction in the free carrier absorption in the infrared region accompanied by the appearance of a shoulder at around ~590 nm associated with the de-doped PBTTT polymer. Re-doping the polymer with the dopant after de-doping recovered the spectra of the initially doped polymer,

**Table 2** Calculated atomic composition ratio of fluorine to carbon (F/C) atoms, the corresponding doping levels, and conductivity values of doped, acetonitrile-treated de-doped, and 120 °C annealed de-doped films.

Sample type	F/C	Doping level (anions per monomer)	Conductivity [S/cm]
Doped	0.106 ± 0.01	0.80 ± 0.08	486 ± 18
Acetonitrile-treated	0.089 ± 0.01	0.67 ± 0.07	255 ± 5
120 °C annealed	0.070 ± 0.01	0.53 ± 0.07	108 ± 6

The F/C ratio was estimated by calculating the area under the F and C XPS spectrum above a linear baseline.

showing the possibility for reversible switching. Similarly, Fig. 3d shows that de-doping via temperature annealing led to a larger reduction in the free carrier absorption, consistent with its lower doping level and conductivity shown in Table 2. Also, in this case, re-doping the polymer could reversibly recover the original optical properties of the doped polymer.

Having demonstrated that the optical material properties of the PBTTT films can be reversibly modulated by controlling their doping state, we use this behavior to actively tune the PBTTT optical nanoantennas. The blue curves in Fig. 3e, f present extinction spectra of doped PBTTT nanoantennas with 90 nm thickness and around 400 nm diameter, showing a plasmonic resonance peak of around 2100 nm. Upon acetonitrile or temperature de-doping, the resonance peak almost disappears due to the lowered doping levels (red and green curves). Additionally, de-doping led to the emergence of the absorption signature around 590 nm of the de-doped PBTTT polymer. Upon re-doping the PBTTT nanodisks, the plasmonic resonance peak recovered to its original state, as shown in the dashed blue curves. Importantly, for both the acetonitrile and temperature annealing de-doping processes, the nano-optical response of the nanodisks could be repeatedly modulated over multiple cycles (see Supplementary Figs. 13, 14).

## Conclusions

We have demonstrated that nanostructures made of the semi-conducting polymer PBTTT doped by the dicationic salt TAB-2TFSI can sustain plasmonic resonances and act as optical nanoantennas. The study thereby expands the field of dynamic organic plasmonics beyond PEDOT-based materials. The PBTTT nanoantennas provide tunable plasmonic behavior based on the polymer being optically metallic in its doped form and dielectric in its undoped form. The plasmonic resonance could be easily controlled from around 2100 nm to around 3200 nm by changing the thickness of nanodisks made from this polymeric material. Furthermore, the nanoantennas could be reversibly tuned by de-doping and re-doping via solvent and temperature treatments. The de-doping treatments modulate the doping levels and provide insights into how doping levels affect plasmonic properties in organic plasmonic nanoantennas. Previous work has shown that PBTTT<sup>40</sup> and other similar polymers<sup>41</sup> can also be electrochemically doped, so making electrically tunable devices would be viable and interesting for future work. Our demonstration that the organic semiconducting polymer PBTTT can sustain plasmonic responses opens the path for the development of other organic plasmonic materials using similarly doped semiconductors, of which there exists a plethora<sup>32–38</sup>. Exciting future possibilities stemming from this work lie in utilizing these types of polymers for their unique tuning functionalities, including tuning by temperature<sup>42</sup> and electrochemical potentials<sup>40,41</sup>. This work thereby establishes a materials platform for tunable

nanooptics, as well as a methodology for the investigation of their nano-optical properties, where future work may, for example, explore structure-property relationships of different types of polymers or dopants.

## Methods

**Materials.** Poly[2,5-bis(3-tetradecylthiophen-2-yl)thieno[3,2-b]thiophene] (PBTTT-C14) and N4,N4,N4',N4'-Tetrakis(4-bromophenyl)-[1,1'-biphenyl]-4,4'-diammonium di[bis(trifluoromethylsulfonyl)imide] (TAB-2TFSI) were synthesized according to previous reports<sup>33,43</sup>.

**Thin film and solution preparation.** Glass substrates (2.5 × 2.5 cm<sup>2</sup>) were cleaned by UV/O3 treatment for 10 min. To prepare a 1.15 mM of TAB-2TFSI dopant solution, 8.18 mg TAB-2TFSI powder was dissolved into 4 mL of anhydrous acetonitrile (<0.001% H<sub>2</sub>O) inside a nitrogen glovebox (<10 ppm O<sub>2</sub>, <2 ppm H<sub>2</sub>O). PBTTT solution was prepared with o-dichlorobenzene (ODCB) solvent by heating at 120 °C for 2 h then 100 °C overnight in N<sub>2</sub> or Ar. Concentration of PBTTT solution was 1 wt% for ~30 nm, 1.5 wt% for ~60 nm, 2 wt% for ~90 nm-thick films. This solution was heated at 120 °C for 1 h before filtering. PBTTT solution was filtered using a glass syringe with a PTFE filter (0.5 µm). Solution, syringe, and filter were kept at 50 °C during the filtering process to avoid damaging the filter. PBTTT solution was spin-coated onto UV/O3 treated glass substrates inside a nitrogen-filled glovebox. The glass substrates were treated with UV/O3 for 10 min. Solution, substrates, and pipettes were heated at 120 °C before spinning. The spinning condition was 500 rpm for 2 s, followed by 2000 rpm for 1 min. Coated samples were heated at 120 °C for 10 min to dry the residual solvent. The samples were then annealed at 180 °C for 1 h, then slowly cooled down.

**Undoped PBTTT nanoantenna fabrication.** A modified version of colloidal lithography was used for the nanodisk array fabrication as shown in Supplementary Fig. 6. To summarize the process, spincoated undoped PBTTT films were treated with a UV-ozone cleaner (UVO-cleaner, model PSD-UV8) for 3 mins to increase the hydrophilicity of the surface. To functionalize the PBTTT surface to be positively charged, 2 wt% poly(diallyldimethylammonium chloride) (PDAA) (522376 (Sigma-Aldrich)) in deionized water was drop-cast onto the film to fully cover it. After 1 min 30 s, the samples were rinsed with deionized water for 40 s, followed by air drying with nitrogen. Negatively charged polystyrene nanoparticles (PS beads, 497 nm, 0.3 wt% in deionized water (Microparticles GmbH, PS-ST KM56-1)) were then dropped on the samples. After 10 min, the samples coated with the PS beads were rinsed with deionized water and dried with a nitrogen stream, which produced a sparse monolayer of PS beads on the undoped PBTTT thin films. This was followed by reactive oxygen plasma etching (250 mtorr, 50 W) for 50–130 s dispensing on the film thickness, using the PS beads monolayer as the mask. Depending on the thicknesses of the PBTTT thin films, the time interval of etching was varied to ensure a complete removal of the PBTTT parts that were not covered by the PS mask. Blue tape was used to remove PS beads to finally produce the undoped PBTTT nanodisks. After the undoped PBTTT nanodisks were fabricated, the disks were doped with the dopant (TAB-2TFSI) inside a nitrogen-filled glovebox with a low moisture content.

**Doping PBTTT nanoantennas.** The doping process was done inside a nitrogen glovebox to avoid the presence of water which can obstruct the doping process. To dope the undoped PBTTT nanoantennas and films, 8 droplets of TAB-2TFSI dopant solution dissolved in acetonitrile from a plastic pipette was dropped onto a substrate spinning at 2000 rpm for 10 s. This changed the color of PBTTT films, indicating that most of doping reaction was completed. After 10 s, the spinning was stopped and the whole surface of the glass substrates containing the nanoantennas were covered with the dopant solution. The dopant solution was left onto the substrate for 1 min to ensure that the films are completely doped. After 1 min, the dopant solution was removed by spinning the substrate at 2000 rpm. The sample was dried at 80 °C for 5 min. To remove any excess dopant that may stick to the glass of the nanoantennas, 2 droplets of acetonitrile solution were dropped onto a substrate spinning at 2000 rpm for 10 s.

**Dedoping PBTTT nanoantennas with acetonitrile and temperature.** 20 droplets of acetonitrile from a plastic pipette were dropped onto a doped PBTT film or nanodisk array spinning at 2000 rpm for 10 s. After stopping the spinning of the substrate, the film was covered by acetonitrile solution for 1 min. After 1 min, the acetonitrile solution was removed by spinning the substrate at 2000 rpm for 1 min. For temperature de-doping, doped films were annealed in air at 120 °C for 1 h.

**UV-Vi-NIR and FTIR spectroscopy.** The extinction spectra of doped and undoped films were measured in air in the vis-NIR range (400–3300 nm) using a UV-vis-NIR spectrometer (Lambda 900 (Perkin Elmer Instruments)) and the in the NIR range (1666–5000 nm) using an Equinox 55 FTIR spectrometer (Bruker). FTIR spectra were acquired in the absorbance mode using a resolution of 4 cm<sup>-1</sup>

and 100 scans. The extinction spectra include transmission losses due to both absorption and scattering.

**Ellipsometry.** Doped and undoped PBTTT films spin-coated on a 2-inch single-side polished *c*-plane sapphire wafer were characterized under normal ambient conditions at room temperature. Spectroscopic ellipsometry data were collected by ellipsometers with different spectral ranges at two to four incident angles (UV-vis-NIR: 0.8–5.9 eV at 40°, 50°, 60°, and 70°; MIR: 0.04–0.80 eV at 40° and 60°; and THz: 0.0028–0.0040 eV at 40°, 50°, and 60°) with were collected by ellipsometers with different spectral ranges at two to four incident angles (UV-vis-NIR - RC2 WASE J. A. Woollam Co.: 0.8–5.9 eV at 40°, 50°, 60°, and 70°; MIR - IR-VASE J. A. Woollam Co., Inc.: 0.04–0.80 eV at 40° and 60°; and THz - an in-house built THz WASE<sup>44</sup> 0.0028–0.0040 eV at 40°, 50°, and 60°). The detailed information of the characterization can be found in our previous studies<sup>29,45</sup>. The obtained data were analyzed by WVASE software (J. A. Woollam Co.) and an anisotropic Drude-Lorentz model was utilized for the films with its thickness determined by an AFM. The extracted permittivity and corresponding fitting parameters for the doped and undoped PBTTT films are shown in the Supplementary Figs. 2–4 and Supplementary Tables 1 and 2 in the Supporting Information.

**Electrical, chemical, and morphological characterization.** Sheet resistance,  $R_s$ , of thin films were measured using a four-point probe set-up with a Signatone Pro4 S-302 resistivity stand and a Keithley 2400. The film thickness  $t$  was determined by Veeco Dimension 3100 AFM. This was used to measure the electrical conductivity of the doped PBTTT films as reported in Table 1. Surface morphology of the nanodisks was obtained by Veeco Dimension 3100 AFM and the images were analyzed using Nanoscope Analysis software (Bruker). X-ray photoemission spectroscopy (XPS) measurements were performed using KRATOS ULTRA 2 with monochromatic Al K $\alpha$  X-rays. The measurements were done in a high vacuum chamber equipped with a turbo molecular pump at a pressure below  $10^{-7}$  Torr. In order to calculate XPS intensity, the area above a linear baseline was estimated. For XPS measurements, 30 nm thick Au was thermally deposited on UV/O<sub>3</sub> treated glass substrates, followed by spin-coating of the PBTTT layer.

**Optical numerical simulations and calculations.** Numerical simulations of the electromagnetic response of doped and undoped PBTTT nanoantennas and films were performed via the finite-difference time-domain (FDTD) method using the commercial software Lumerical FDTD Solutions (<http://www.lumerical.com/fdtd.php>). The optical parameters for the doped and undoped thin films were taken as the anisotropic complex permittivity obtained from the ellipsometry measurements. For periodic nanodisk arrays and thin films, the spectra and near-field profiles were recorded via field and power monitors. Periodic PBTTT nanodisk arrays (or thin film) were placed on top of the glass substrates ('SiO<sub>2</sub>-Palik' from Lumerical FDTD Solutions). The structures were illuminated by a plane wave light source at normal incidence. Antisymmetrical and symmetrical boundaries were used for the  $x$  axis (parallel to the polarization) and  $y$  axis (normal to the polarization) and perfectly matched layers were used for the  $z$  axis (parallel to the light incident direction). The mesh size was  $2 \times 2 \times 2$  nm<sup>3</sup>. The optical parameter for glass was taken from the literature<sup>46</sup>.

## Data availability

The datasets generated during and/or analyzed during the current study are available from the corresponding author upon reasonable request.

Received: 18 March 2022; Accepted: 21 June 2022;

Published online: 14 July 2022

## References

- Novotny, L. & van Hulst, N. Antennas for light. *Nat. Photonics* **5**, 83–90 (2011).
- Shi, X. et al. Enhanced water splitting under modal strong coupling conditions. *Nat. Nanotechnol.* **13**, 953–958 (2018).
- Atwater, H. A. & Polman, A. Plasmonics for improved photovoltaic devices. *Nat. Mater.* **9**, 205–213 (2010).
- Sheldon, M. T., Groep, J. V. D., Brown, A. M., Polman, A. & Atwater, H. A. Plasmoelectric potentials in metal nanostructures. *Science* **346**, 828–831 (2014).
- Yesilkoy, F. et al. Phase-sensitive plasmonic biosensor using a portable and large field-of-view interferometric microarray imager. *Light Sci. Appl.* **7**, 17152–17152 (2018).
- Mazzotta, F., Wang, G., Hägglund, C., Höök, F. & Jonsson, M. P. Nanoplasmonic biosensing with on-chip electrical detection. *Biosens. Bioelectron.* **26**, 1131–1136 (2010).
- Jonsson, M. P., Dahlin, A. B., Jönsson, P. & Höök, F. Nanoplasmonic biosensing with focus on short-range ordered nanoholes in thin metal films (Review). *Biointerphases* **3**, FD30–FD40 (2008).
- Jonsson, M. P., Jönsson, P., Dahlin, A. B. & Höök, F. Supported Lipid Bilayer Formation and Lipid-Membrane-Mediated Biorecognition Reactions Studied with a New Nanoplasmonic Sensor Template. *Nano Lett.* **7**, 3462–3468 (2007).
- Englebienne, P. Use of colloidal gold surface plasmon resonance peak shift to infer affinity constants from the interactions between protein antigens and antibodies specific for single or multiple epitopes. *Analyst* **123**, 1599–1603 (1998).
- Shao, L., Zhuo, X. & Wang, J. Advanced Plasmonic Materials for Dynamic Color Display. *Adv. Mater.* **30**, 1704338 (2018).
- Franklin, D., Frank, R., Wu, S.-T. & Chanda, D. Actively addressed single pixel full-colour plasmonic display. *Nat. Commun.* **8**, 15209 (2017).
- Xiong, K. et al. Plasmonic Metasurfaces with Conjugated Polymers for Flexible Electronic Paper in Color. *Adv. Mater.* **28**, 9956–9960 (2016).
- Xiong, K., Tordera, D., Jonsson, M. P. & Dahlin, A. B. Active control of plasmonic colors: emerging display technologies. *Rep. Prog. Phys.* **82**, 024501 (2019).
- Park, J., Kang, J.-H., Kim, S. J., Liu, X. & Brongersma, M. L. Dynamic Reflection Phase and Polarization Control in Metasurfaces. *Nano Lett.* **17**, 407–413 (2017).
- Chen, X. et al. Dual-polarity plasmonic metalens for visible light. *Nat. Commun.* **3**, 1198 (2012).
- Aieta, F. et al. Aberration-Free Ultrathin Flat Lenses and Axicons at Telecom Wavelengths Based on Plasmonic Metasurfaces. *Nano Lett.* **12**, 4932–4936 (2012).
- Pendry, J. B. Negative Refraction Makes a Perfect Lens. *Phys. Rev. Lett.* **85**, 3966–3969 (2000).
- Yu, N. et al. Light Propagation with Phase Discontinuities: Generalized Laws of Reflection and Refraction. *Science* **334**, 333–337 (2011).
- Naik, G. V., Shalae, V. M. & Boltasseva, A. Alternative Plasmonic Materials: Beyond Gold and Silver. *Adv. Mater.* **25**, 3264–3294 (2013).
- Wang, Y. et al. Electrical tuning of phase-change antennas and metasurfaces. *Nat. Nanotechnol.* 1–6, <https://doi.org/10.1038/s41565-021-00882-8> (2021).
- Alaee, R., Albooyeh, M., Tretyakov, S. & Rockstuhl, C. Phase-change material-based nanoantennas with tunable radiation patterns. *Opt. Lett.* **41**, 4099–4102 (2016).
- Wuttig, M., Bhaskaran, H. & Taubner, T. Phase-change materials for non-volatile photonic applications. *Nat. Photonics* **11**, 465–476 (2017).
- Kim, Y. et al. Phase Modulation with Electrically Tunable Vanadium Dioxide Phase-Change Metasurfaces. *Nano Lett.* **19**, 3961–3968 (2019).
- Abdollahramezani, S. et al. Tunable nanophotonics enabled by chalcogenide phase-change materials. *Nanophotonics* **9**, 1189–1241 (2020).
- Liu, Z. et al. Tuning infrared plasmon resonances in doped metal-oxide nanocrystals through cation-exchange reactions. *Nat. Commun.* **10**, 1394 (2019).
- Fang, Z. et al. Gated Tunability and Hybridization of Localized Plasmons in Nanostructured Graphene. *ACS Nano* **7**, 2388–2395 (2013).
- Yan, H. et al. Tunable infrared plasmonic devices using graphene/insulator stacks. *Nat. Nanotechnol.* **7**, 330–334 (2012).
- Ju, L. et al. Graphene plasmonics for tunable terahertz metamaterials. *Nat. Nanotechnol.* **6**, 630–634 (2011).
- Chen, S. et al. Conductive polymer nanoantennas for dynamic organic plasmonics. *Nat. Nanotechnol.* **15**, 35–40 (2020).
- Karst, J. et al. Electrically switchable metallic polymer nanoantennas. *Science* **374**, 612–616 (2021).
- Karki, A. et al. Electrical Tuning of Plasmonic Conducting Polymer Nanoantennas. *Adv. Mater.* **34**, 2107172 (2022).
- Jacobs, I. E. et al. High-Efficiency Ion-Exchange Doping of Conducting Polymers. *Adv. Mater.* **34**, 2102988 (2021).
- Kurosawa, T. et al. Strong and Atmospherically Stable Dicationic Oxidative Dopant. *Adv. Sci.* **n/a**, e2101998 (2021).
- Yamashita, Y. et al. Supramolecular cocrystals built through redox-triggered ion intercalation in  $\pi$ -conjugated polymers. *Commun. Mater.* **2**, 1–9 (2021).
- Yamashita, Y. et al. Efficient molecular doping of polymeric semiconductors driven by anion exchange. *Nature* **572**, 634–638 (2019).
- Yurash, B. et al. Towards understanding the doping mechanism of organic semiconductors by Lewis acids. *Nat. Mater.* **18**, 1327–1334 (2019).
- Thomas, E. M. et al. Effects of Counter-Ion Size on Delocalization of Carriers and Stability of Doped Semiconducting Polymers. *Adv. Electron. Mater.* **6**, 2000595 (2020).
- Kohn, S. et al. Controlled steric selectivity in molecular doping towards closest-packed supramolecular conductors. *Commun. Mater.* **1**, 1–8 (2020).
- Sanz, J. M. et al. UV Plasmonic Behavior of Various Metal Nanoparticles in the Near- and Far-Field Regimes: Geometry and Substrate Effects. *J. Phys. Chem. C* **117**, 19606–19615 (2013).

40. Tanaka, H. et al. Thermoelectric properties of a semicrystalline polymer doped beyond the insulator-to-metal transition by electrolyte gating. *Sci. Adv.* **6**, eaay8065 (2020).
41. Herlogsson, L., Crispin, X., Tierney, S. & Berggren, M. Polyelectrolyte-Gated Organic Complementary Circuits Operating at Low Power and Voltage. *Adv. Mater.* **23**, 4684–4689 (2011).
42. Yuan, D. et al. Quinoid-Resonant Conducting Polymers Achieve High Electrical Conductivity over 4000 S cm<sup>−1</sup> for Thermoelectrics. *Adv. Sci.* **5**, 1800947 (2018).
43. McCulloch, I. et al. Liquid-crystalline semiconducting polymers with high charge-carrier mobility. *Nat. Mater.* **5**, 328–333 (2006).
44. Kühne, P. et al. Advanced Terahertz Frequency-Domain Ellipsometry Instrumentation for In Situ and Ex Situ Applications. *IEEE Trans. Terahertz Sci. Technol.* **8**, 257–270 (2018).
45. Chen, S. et al. On the anomalous optical conductivity dispersion of electrically conducting polymers: ultra-wide spectral range ellipsometry combined with a Drude–Lorentz model. *J. Mater. Chem. C* **7**, 4350–4362 (2019).
46. Palik, E. D. *Handbook of optical constants of solids* (Academic Press, 1985).

## Acknowledgements

The authors acknowledge financial support from the Knut and Alice Wallenberg Foundation, the Swedish Research Council (2020-00287), the Swedish Foundation for Strategic Research (SSF), and the Swedish Government Strategic Research Area in Materials Science on Functional Materials at Linköping University (Faculty Grant SFO-Mat-LiU No 2009 00971). M.P.J. is a Wallenberg Academy Fellow. The authors would like to thank Giancarlo Cincotti for helpful discussions.

## Author contributions

The work was planned and proceeded by discussions among M.P.J., A.K., S.W. and Y.Y. A.K. conducted the colloidal lithography on films to make the nanodisks, did the doping of the films and nanodisks, measured the optical spectroscopy (UV-vis and FTIR) of films and nanodisks, and did the ellipsometry data fitting and optical simulations. Y.Y. prepared the undoped films, conducted XPS measurements and tuning of doping conditions in films. S.C. measured ellipsometry of the films in the UV-visible and mid-infrared range and did the ellipsometry data fitting and optical simulations. T.K. synthesized the employed dopants and polymers. J.T. supervised preparation and electrical evaluation of dopants and doped polymers. V.S. and V.D. measured ellipsometry of films in the far-infrared and terahertz range. M.P.J. and A.K. finalized the manuscript with inputs from all the authors.

## Funding

Open access funding provided by Linköping University.

## Competing interests

The authors declare no competing interests. Shun Watanabe is an Editorial Board Member for *Communications Materials* and was not involved in the editorial review of, or the decision to publish, this Article.

## Additional information

**Supplementary information** The online version contains supplementary material available at <https://doi.org/10.1038/s43246-022-00268-w>.

**Correspondence** and requests for materials should be addressed to Magnus P. Jonsson.

**Peer review information** *Communications Materials* thanks the anonymous reviewers for their contribution to the peer review of this work. Primary Handling Editor: Aldo Isidori. Peer reviewer reports are available.

**Reprints and permission information** is available at <http://www.nature.com/reprints>

**Publisher's note** Springer Nature remains neutral with regard to jurisdictional claims in published maps and institutional affiliations.



**Open Access** This article is licensed under a Creative Commons Attribution 4.0 International License, which permits use, sharing, adaptation, distribution and reproduction in any medium or format, as long as you give appropriate credit to the original author(s) and the source, provide a link to the Creative Commons license, and indicate if changes were made. The images or other third party material in this article are included in the article's Creative Commons license, unless indicated otherwise in a credit line to the material. If material is not included in the article's Creative Commons license and your intended use is not permitted by statutory regulation or exceeds the permitted use, you will need to obtain permission directly from the copyright holder. To view a copy of this license, visit <http://creativecommons.org/licenses/by/4.0/>.

© The Author(s) 2022